Single-Arm Frequency-Shifted Interferometry Using a Bidirectional Electro-Optic Modulator

Huiyong Guo, Amita Gnanapandithan, Yi Liu, Ciming Zhou, Zhou Zheng, Yiwen Ou, Xiong Zeng, and Li Qian

***Abstract*—Multiplexing fiber-optic sensors is an effective way to perform large-area quasi-distributed sensing. Among many sensor multiplexing and interrogation methods, frequency-shifted interferometry (FSI) emerges as a unique low-cost technique that is capable of resolving sensor locations using a continuous-wave broadband source, a bidirectional optical frequency shifter, and a slow photo detector. An acousto-optic modulator is typically used as the frequency shifter in FSI due to its high modulation efficiency and bidirectional operation. But its relatively low modulation bandwidth results in low spatial resolution, on the order of meters. To improve spatial resolution, single-arm FSI (SA-FSI) that employs an electro-optic modulator (EOM) as the frequency shifter was proposed, but the EOM's broad modulation bandwidth cannot be fully utilized because conventional EOMs cannot support bidirectional modulation at gigahertz frequencies due to the speed mismatch between the optical wave and the applied RF wave, especially when the two are counter propagating. In this paper, we modified a commercial EOM to increase the modulation efficiency of the counter-propagating optical wave and used it to interrogate 15 weak fiber Bragg gratings (FBGs) in an array, achieving a spatial resolution of $\sim$3 cm and a sensing range of $>$1 km. A signal-to-noise ratio as high as $\sim$18 dB was obtained with a 15-mW broadband amplified spontaneous emission source without any optical amplification. This is the first demonstration of both spatially resolved and spectrally resolved SA-FSI, and it is the first time that FBGs are interrogated with the SA-FSI technique.**

***Index Terms*—Fiber Bragg gratings, fiber-optic sensing, frequency-shifted interferometry, sensor array multiplexing.**

Manuscript received October 11, 2018; revised January 1, 2019; accepted January 7, 2019. Date of publication January 11, 2019; date of current version February 22, 2019. This work was supported in part by the National Natural Science Foundation of China under Grant 61735013; in part by the Natural Science Foundation of China under Grant 61775173; in part by the The National Key Research and Development Program of China under Grant 2017YFB0405500; in part by the Grand Science and Technology Special Project in Hubei Province under Grant 2016AAA008; in part by the Canada Foundation for Innovation (Project 203429); and in part by the Natural Science and Engineering Research Council of Canada under Grants RGPIN-2014-06425 and RGPAS 462021-2014). *(Corresponding author: Li Qian.)*

H. Guo and L. Qian are with the Department of Electrical and Computer Engineering, University of Toronto, Toronto, ON M5S 3G4, Canada, and also with the National Engineering Laboratory for Fiber Optic Sensing Technology, Wuhan University of Technology, Wuhan 430070, China (e-mail: ghylucky@whut.edu.cn; l.qian@utoronto.ca).

A. Gnanapandithan and Y. Liu are with the Department of Electrical and Computer Engineering, University of Toronto, Toronto, ON M5S 3G4, Canada (e-mail: amita.gnanapandithan@mail.utoronto.ca; wgdliuyi2001@126.com).

C. Zhou, Z. Zheng, Y. Ou, and X. Zeng are with the National Engineering Laboratory for Fiber Optic Sensing Technology, Wuhan University of Technology, Wuhan 430070, China (e-mail: zcm@whut.edu.cn; 974172272@qq.com; ouyiwen2013@whut.edu.cn; 307894226@qq.com).

Color versions of one or more of the figures in this paper are available online at http://ieeexplore.ieee.org.

Digital Object Identifier 10.1109/JLT.2019.2892373

I. Introduction

OPTICAL sensing using fiber Bragg grating (FBG) arrays is one of the most commonly employed method to achieve multi-point sensing, such as in structural health monitoring [1]–[3] and temperature sensing [4]. Frequency shifted interferometry (FSI) [5] has emerged in recent years as a practical technique to interrogate fiber-optic sensor arrays [6], [7]. Utilizing asymmetric frequency shifts in a common-path interferometer, FSI can perform location-resolved sensing using a low cost broadband source and a slow detector [5]. Compared to the wavelength-division multiplexing (WDM) technique [8] for sensor multiplexing, FSI can work with FBGs reflecting in the same (or different) wavelength regions, significantly increasing the dynamic range of the FBG sensors, as well as reducing the fabrication cost of the FBG arrays. Compared to the time-division-multiplexing (TDM) techniques [9], FSI does not require short pulse laser sources, optical amplifiers, or high-speed detectors, significantly reducing the cost of the overall system. Compared to the more recently reported optical-carrier-based microwave interferometry (OCMI) [10], FSI does not require high-bandwidth detectors, nor does it require any hardware for vector analysis in the microwave domain. FSI exhibits a number of similarities with frequency-domain optical reflectometry (OFDR) [11], but unlike OFDR which requires a reference beam for interference, FSI is based on self-interference (or common-path interference) where the two interfering beams go through exactly the same optical path. As a result, FSI can use incoherent, non-polarized light sources for location-resolved sensing. The combination of these advantages, namely, relaxed requirements on FBG fabrication, polarization-insensitivity, the use of a low-cost slow detector, and the use of continuous-wave incoherent light source without the need for amplification, makes FSI an attractive new technology rivaling WDM, TDM, OCMI, and OFDR technologies. Recently, FSI has been employed to interrogate a large array of hundreds of FBGs [12], demonstrating its potential for practical applications.

The conventional FSI uses a Sagnac loop with an acousto-optic modulator (AOM) as the frequency shift element [13]. With this implementation, FSI has a spatial resolution limited by the modulation bandwidth of the AOM. For example, if the AOM modulation bandwidth is 20 MHz (from 90 MHz – 110 MHz), the theoretical spatial resolution of the resulting AOM is 5 m [14]. Single-arm FSI (SA-FSI) [15], [16] employing an electro-optical modulator (EOM) not only has a simpler configuration, it

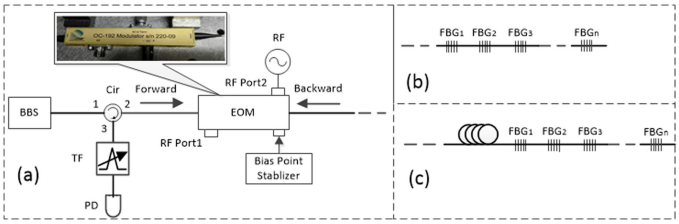

Fig. 1. (a) Experimental setup of SA-FSI with a broadband source (BBS), an optical circulator (Cir), an electro-optical modulator (EOM), a tunable filter (TF), and a slow photo-detector (PD). (b) An array of 15 fiber Bragg gratings (FBGn). (c) 1 km fiber followed by the same 15-FBG array.

can also take advantage of the GHz modulation bandwidth of the EOM to achieve orders-of-magnitude higher spatial resolution.

However, the SA-FSI requires bidirectional modulation of the EOM. Due to the mismatch of the propagation speeds between the RF wave and the optical wave inside the EOM [17], its modulation efficiency is drastically different for the co-propagating and the counter-propagating optical wave (with respect to the propagating RF wave) when the RF frequency is increased beyond 2 GHz or so. For this reason, the modulation bandwidth in [16] was limited to 1 GHz, leading to the coarse spatial resolution of 30 cm. The signal strength for [16] also suffers due to low modulation efficiency. As a result, only broadband facet reflections were detected, and no demonstration of narrow-band FBG multiplexing was attempted using SA-FSI so far.

In this paper, we demonstrate SA-FSI with bidirectional EOM modulation with a modulation bandwidth of 6 GHz (ranging from 2 GHz to 8 GHz), providing a spatial resolution of ~3 cm. The bidirectional modulation is made more efficient by removing the termination impedance of the EOM, creating a reflection of the RF wave at the termination. As a result, much higher modulation efficiency was achieved for the counter-propagating optical wave. Using this bidirectional EOM, we demonstrate multiplexing of 15 spectrally overlapped FBGs in a series with centimeter spacing between adjacent gratings. We obtained the reflection spectrum of each of the gratings using a tunable filter before the detector. Therefore, spectrally and spatially resolved interrogation of near identical FBGs in an array is achieved for the first time using an incoherent light source.

II. Principle of Operation

A generic SA-FSI configuration is illustrated in Fig. 1(a). The output of a continuous wave (CW) broadband source (BBS), typically an ASE source, is first modulated by an EOM before propagating down the fiber sensor array. The reflected light from the sensors propagates in the backward direction through the EOM and is modulated a second time. Either amplitude or phase modulation can be used, because the purpose of modulation is to create frequency sidebands. The driving RF frequency of the EOM is swept during a measurement, and both spectral and location information of the sensors can be obtained by detecting the reflected spectral light intensity as a function of the RF frequency.

The principle of operation and mathematical derivation can be found in [16], but [16] did not take into account of the different modulation efficiencies experienced by the co- and counter-propagating optical waves. Here, we briefly summarize the approach taken in [16] and introduce new analysis to account for the frequency-dependent modulation efficiencies due to the speed mismatch between the optical and the RF wave, for both co- and counter-propagating optical waves. The frequency-dependent modulation efficiencies in both cases can be determined experimentally (see next section), and are used to verify our analysis.

The output of an incoherent broadband source (Fig. 1(a)) can be considered as a summation of narrow-band frequency components. For each frequency component, the RF modulation of the EOM creates frequency-shifted sidebands. The amount of frequency shift is equal to the RF driving frequency, *f*. Both the sidebands and the baseband propagate down the fiber and are reflected by various sensors. When the reflected light from the i^{th} sensor is returned to the EOM, new sidebands will be generated. In other words, the old sidebands were generated when light is propagating in the forward direction, while the new sidebands are generated later, when the reflected light is propagating in the backward direction. The phase difference between the old and the new sidebands is $\Delta\psi_i = 2\pi(2nL_i/c)\,f$, where *n* is the effective index of the fiber mode, L_i is the distance between the i^{th} sensor and the EOM, *c* is the speed of light, and *f* is the RF frequency, positive for the upshifted sidebands and negative for the downshifted sidebands. The detected intensity (I_ν) at the optical frequency ν contains the interference between the old and the new sidebands. Assuming an amplitude modulator is used, driven by sinusoidal RF waves, then I_ν has the following general form [16]:

$$I_\nu(f) \propto DC + \mathrm{J}_0^2\left(\alpha\tfrac{\pi}{2}\right)\mathrm{J}_1^2\left(\alpha\tfrac{\pi}{2}\right) \cdot \sin^2(\pi\varepsilon)\sum_i R_i(\nu)\cos\left(2\pi\tfrac{2nL_i}{c}f\right) \quad (1)$$

where J_0, J_1 are the Bessel functions of the first kind of order 0 and 1, respectively, $\alpha = V_{RF}/V_\pi$ is the modulation depth defined by the ratio of the applied RF voltage amplitude V_{RF} to the half-wave voltage V_π of the EOM, $\varepsilon = (V_{\text{bias}}–V_{\min})/V_\pi$ is the bias parameter related to the DC bias voltage V_{bias} to the modulator (where $V_{\min}$ is the bias voltage at which the EOM's output is minimized), and $R_i(\nu)$ is the reflectivity of the i^{th} sensor at the optical frequency ν. The first DC term in (1) is the constant background intensity. In deriving (1), only the first-order sidebands are kept, and higher-order terms are omitted. From (1) one can see that the spectral information of the sensor $R_i(\nu)$ is contained in the amplitude of the detected signal, while the location information L_i is contained in the phase.

Equation (1) derived in [16] assumes that the modulation depth α and the bias parameter ε are independent of RF frequency *f*, and independent of the direction of propagation of the optical wave. While the DC bias parameter ε is independent of frequency, the modulation depth α does in fact vary with frequency *f*, because of material dispersion (i.e., frequency dependence of the electro-optic coefficient) and more importantly, because of the frequency-dependent speed mismatch between the RF modulating wave and the optical wave. The speed mismatch is different for co-propagating and counter-propagating optical waves, with respect to the propagating direction of the RF wave. We therefore introduce

an *effective* V_π that is frequency-dependent and direction-dependent, denoted as $V_{F,B\_\pi}(f)$, where F and B refers to the forward and backward propagation, respectively. As a result, the modulation depth is also a function of frequency and propagation direction, which is denoted by $\alpha_{\mathrm{F,B}}(f)$. Equation (1) then needs to be modified as:

$$I_v(f) \propto DC + \mathrm{J}_0\left(\alpha_F \tfrac{\pi}{2}\right)\mathrm{J}_0\left(\alpha_B \tfrac{\pi}{2}\right)\mathrm{J}_1\left(\alpha_F \tfrac{\pi}{2}\right)\mathrm{J}_1\left(\alpha_B \tfrac{\pi}{2}\right) \cdot \sin^2(\pi\varepsilon)\sum_i R_i(\nu)\cos\left(2\pi\tfrac{2nL_i}{c}f + \varphi(f)\right) \tag{2}$$

where

$$\alpha_{F,B}(f) = \frac{V_{RF}}{V_{F,B\_\pi}(f)} \tag{3}$$

and $\varphi(f)$, an additional phase factor due to the speed mismatch, varies slowly with the RF driving frequency f. For simplicity, we will leave out effect of $\varphi(f)$ in the subsequent discussion. In (3), the effective half-wave voltage, $V_{F,B\_\pi}(f)$, in the presence of speed mismatch is

$$V_{F,B\_\pi}(f) = \frac{V_\pi(f)}{\mathrm{sinc}(\pi f \Delta t_{F,B})} \tag{4}$$

where $\Delta t_{F,B} = |v_{RF} - v_{opt}|L_{EOM}/(v_{RF}\, v_{opt})$, and v_{RF} and v_{opt} are the propagation speeds of the RF and the optical wave, respectively, inside the EOM of length L_{EOM}. The physical interpretation for $\Delta t_{F,B}$ is the amount of temporal walk-off between the optical wave and the RF wave after propagating through the modulator. Note, in this convention v_{opt} is positive for co-propagation and negative for counter-propagation. When RF wave is applied in the backward direction, as is the case in our experiment (Fig. 1(a)), v_{opt} is negative (positive) for the forward (backward) propagating optical wave. With a larger speed mismatch $|v_{RF} - v_{opt}|$, as in the case of counter-propagation, the effective half-wave voltage increases, and the modulation depth decreases.

While the modulation depth α determines the strength of the interference signal I_v in (2), a more intuitive parameter to describe the modulation efficiency, which is also experimentally measurable, is [19]

$$\eta_{F,B}(f) = 2\mathrm{J}_1^2\left(\alpha_{F,B}\frac{\pi}{2}\right) \tag{5}$$

which is the ratio of the sideband optical power (when $\mathrm{V_{bias}} = \mathrm{V_{min}}$) to the input optical power. In deriving (5), we consider the input optical E field as $\mathrm{E_o}\cos(\omega t)$, and the RF driving field as $\mathrm{V_{RF}}\sin(2\pi ft)$. Then, when the EOM is biased at minimum, the output optical E field is [19] $\mathrm{E_o}\sin(\alpha_{\mathrm{F,B}}\pi\sin(2\pi ft)/2)\sin(\omega t + \phi)$. Using the approximation that $\sin(x\sin\theta) = 2\mathrm{J}_1(x)\sin\theta$, we arrive at (5). Fig. 2(a) shows the simulated modulation efficiency for the co- and counter-propagating optical waves. One can see that the modulation efficiency for the counter-propagating optical wave is at least 13 dB lower than for the co-propagating case. This is due to the vastly different effective half-wave voltages for the two cases, as expressed by (4). The much reduced modulation efficiency for the counter-propagating optical wave results in much reduced interference signal strength obtained by FSI.

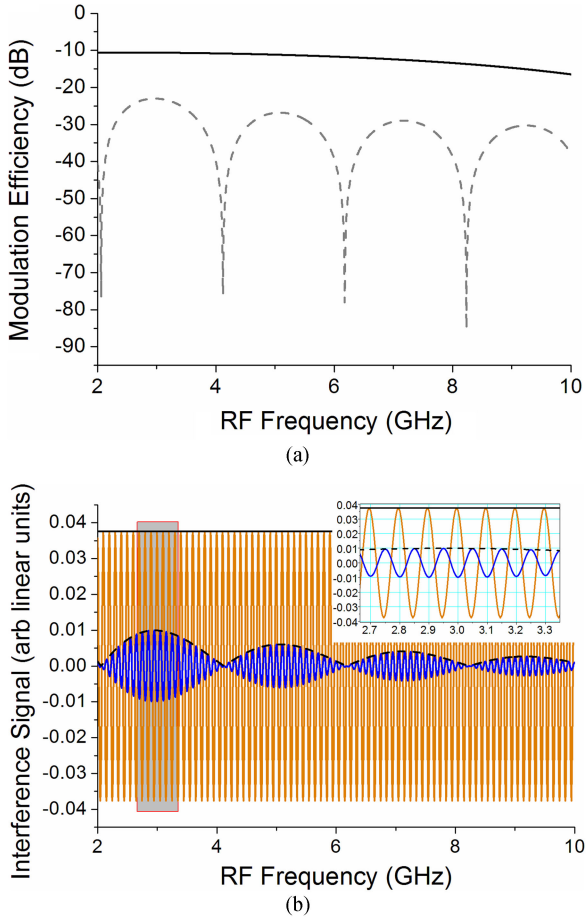

Fig. 2. (a) Simulated modulation efficiency for co-propagating (solid line) and counter-propagating (dashed line) optical waves as a function of frequency, according to (3)–(5). (b) The simulated interference signals as expressed by the AC terms in (2) (blue) and (1) (orange), respectively. The blue curve shows a reduced signal strength as well as a frequency-dependence, both are the result of considering speed mismatch. The envelopes of the interference signals, referred to as the signal strength, is also plotted for the two cases in black solid and dashed lines, which correspond to the product of the Bessel functions in (1) and in (2), respectively. The following simulation parameters are used: $\mathrm{V_{RF}} = 1.5$ V, $\mathrm{V}_\pi = 5.7$ V, the length of the EOM (L_{EOM}) is 3.1 cm, and the speed mismatch $|v_{RF} - v_{opt}|$ is $0.87c$ and $0.13c$ for counter- and co-propagation, respectively, where c is the speed of light in vacuum.

In Fig. 2(b), we compare the interference signal strengths, with and without considering speed mismatch, as defined by the second term (the AC term) of (2) and of (1), respectively. Ref [16] did not consider the speed mismatch, and the AC signal amplitude in (1) is simply $\mathrm{J_0}^2(\alpha\pi/2)\mathrm{J_1}^2(\alpha\pi/2)$, independent of frequency (solid black line in Fig. 2(b)). However, after including the speed mismatch, the signal amplitude in (2) becomes $\mathrm{J_0}(\alpha_{\mathrm{F}}\pi/2)\mathrm{J_0}(\alpha_{\mathrm{B}}\pi/2)\mathrm{J_1}(\alpha_{\mathrm{F}}\pi/2)\mathrm{J_1}(\alpha_{\mathrm{B}}\pi/2)$ (dashed black line in Fig. 2(b)). There are two effects as the result of including speed mismatch in our model: One is that the overall signal strength is lower, due to the much reduced modulation efficiency for the counter-propagating optical wave; The second effect is that there is a frequency-dependent amplitude modulation (or envelope) on the interference signal. In practice, as this amplitude modulation has an oscillation period much larger than those corresponding to the cosine terms in (2), this amplitude modulation effect can be removed in data post processing. However, the first

effect, i.e., the reduced signal strength, is still a critical problem to be addressed.

To improve signal strength, we use passive RF reflection inside the EOM, causing RF waves to propagate both in the forward and backward direction. We will show experimentally and through simulation that this indeed results in a significant improvement to the signal strength in the next section.

The sensing range and spatial resolution of the SA-FSI has the same form as the conventional FSI and are discussed in detail in [5]. For reader's convenience, we provide the formula for the sensing range L_{range}:

$$L_{range} = \frac{c}{4nf_{step}} \tag{6}$$

where f_{step} is the RF frequency step taken in the measurement. As well, the formula for the spatial resolution δL is

$$\delta L = \frac{c}{2n\Delta f} \tag{7}$$

where f is the RF frequency sweep range.

From (7) we can easily see that the large modulation bandwidth of the EOM allows us to access multi-gigahertz of frequency sweep range (Δf), greatly increase the spatial resolution of the technique. However, this comes with a condition: that the EOM must be able to operate bi-directionally over the large frequency sweep range. In other words, the EOM must maintain sufficient modulation efficiency for both forward and backward propagating lightwaves.

III. Experiment

A. Experimental Characterization of a Bi-Directional EOM

The bidirectional EOM we use (Micro Photonix Integration OC-192) has two RF ports, in addition to a DC bias port (see Fig. 1(a) inset). The two-RF-port configuration allows the user to input RF waves either in the forward or backward direction. Normally the unused port should be terminated with a 50 Ω impedance to minimize reflection of the RF power, making the EOM a uni-directional device. Only the optical wave that is co-propagating with the RF wave will be efficiently modulated. In our case, however, to use it for bidirectional modulation, we intentionally leave the unused port open circuit to create a strong reflection of the RF power, such that both forward and backward propagating optical wave will be modulated.

The modulation efficiencies of the EOM for both forward and backward propagating optical waves are characterized as a function of RF driving frequency, and compared to simulation results (Fig. 3). We applied the RF driving signal from an RF signal generator (HP83620B) with its output set to 15 dBm to RF Port 2 of the EOM (Fig. 1(a)). The frequency is tuned from 2.0 GHz to 10 GHz. We bias our EOM at minimum transmission using an automatic bias feedback circuit (PlugTech MBC-MZM-01), and measure the ratio of the output sideband light power with modulation to the output light power without modulation. (Note this is the same definition as in (5), except the insertion loss of the EOM is calibrated out.) We measured the modulation efficiencies while varying the RF frequency for all four cases,

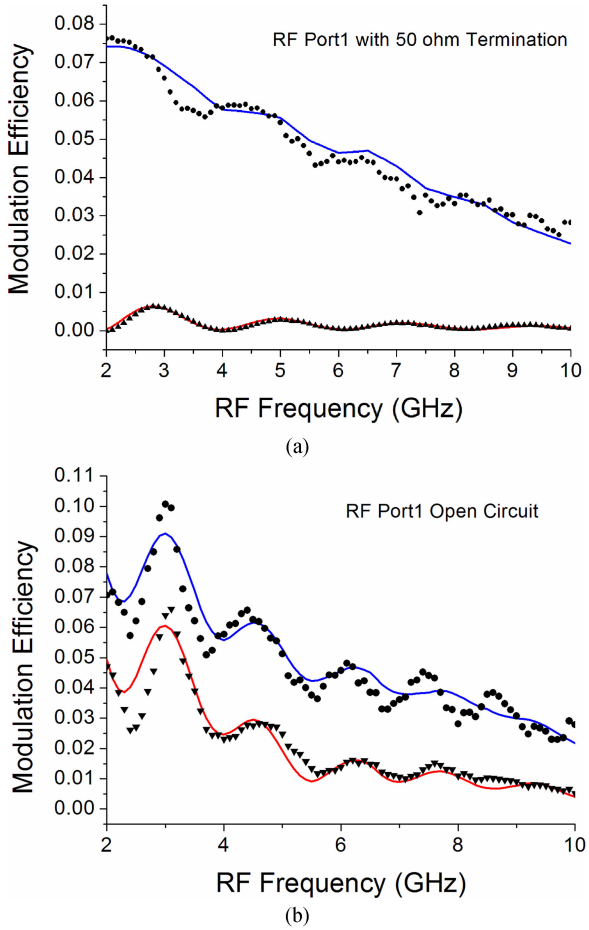

Fig. 3. Measured (symbol) and simulated (line) modulation efficiencies of the EOM (a) with and (b) without 50 Ω termination. The co-propagation (optical wave is backward) cases are illustrated with circles and blue lines, and the counter-propagation cases (optical wave is forward) are with the triangles and red lines. The nominal incident RF power is 15 dBm and the indicident optical power is −2.0 dBm. The EOM is biased at minimum. A (a) 2% and (b) 100% RF power reflection is assumed in the simulation for the case with and without 50 Ω termination, respectively. The simulation uses the measured RF incident power to the EOM, and account for the RF power loss through the EOM. Other parameters used in the simulation are: $V_\pi(f) = 5.7\ V - 0.2f$, where f is the RF frequency (in GHz). $L_{EOM} = 3.1$ cm, $|v_{RF} - v_{opt}|$ is $0.87c$ and $0.13c$ for counter- and co-propagation, respectively, where c is the speed of light in vacuum.

separately: forward optical waves in EOM with 50 Ω termination at RF Port 1 (Fig. 3(a)); backward optical waves in EOM with 50 Ω termination at RF Port 1 (Fig. 3(a)); forward optical waves in EOM without 50 Ω termination at RF Port 1, i.e., open circuit (Fig. 3(b)); backward optical waves in EOM without 50 Ω termination at RF Port 1 (Fig. 3(b)). For calibration and simulation purposes, we also measure the incident and transmitted RF voltages through the EOM.

Based on (3) and (4), we have developed a simulation model for the modulation efficiencies in the presence of speed mismatch and RF reflection. In our model, the RF reflection is included such that the optical wave is modulated by RF waves in both directions. For co-propagating optical and RF waves, the speed mismatch is moderate, but for counter-propagating optical and RF waves, the speed mismatch is large. In addition, RF reflection coefficient and RF loss along the waveguide can be included in the model. We use the following physical parameters

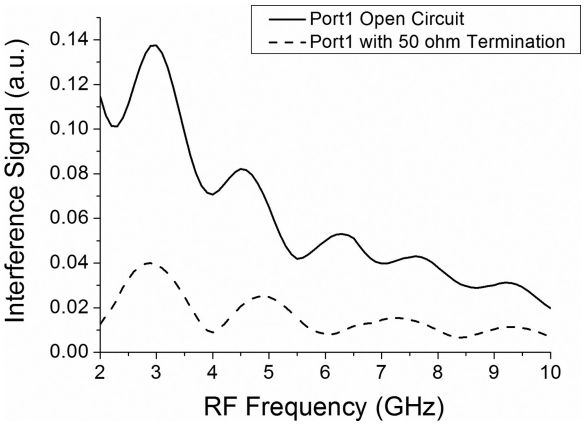

Fig. 4. The simulated SA-FSI signal strength, or equivalently, the envelope of the interference signal, with (dashed line) and without (solid line) 50 Ω termination at RF Port 1, using measured parameters obtained from Fig. 3.

of the EOM to fit the model calculation with the experimental data: The length of the EOM waveguide 3.1 cm, which corresponds to the physical measurement of the length between the two RF ports (Fig. 1(a) inset). The RF propagation speed used is $0.37c$, and the optical propagation speed is $0.5c$, corresponding to an effective refractive index of 2.0 for the optical mode. The $0.37c$ is selected to best fit the simulation data with experimental data presented in Fig. 3. The RF reflectance is assumed to be 2% and 100% for with and without termination, respectively. A frequency-dependent RF loss (from 3 dB at 2 GHz to 7.6 dB at 10 GHz, based on experimental measurements) is also included in the model. The half-wave voltage V_π used in the simulation is 5.7 V at DC and linearly drops to 3.7 V at 10 GHz. These values are largely in line with commercial $LiNbO_3$-based EOMs [20] and manufacturer's data sheet. Therefore, all of the fitting parameters used by the simulation are realistic for the EOM and consistent with those reported in the literature.

The measured and simulated modulation efficiencies are to a large extent in good agreement (Fig. 3). The small discrepancies between the simulation and the measurement can be attributed to several factors: The measured RF voltage may not represent the actual voltage applied onto the EOM waveguide due to loss and frequency response of the RF cables and connectors, and the simulation uses a uniform voltage (which is the average of the incident and transmitted RF voltage) along the waveguide, instead of a decaying voltage due to RF power loss. In the cases where the EOM is not terminated (open circuit at RF port 1), the simulation takes into account of only one reflection, whereas multiple reflections of RF waves can be at play since the RF wave reflected at RF port 1 can be reflected again at the RF source. (This second reflection can be eliminated using an RF circulator between the source and the EOM in the future.) Despite these factors, the good agreement between the simulation and experiment gives us confidence on the physical EOM parameters we used to fit the experimental data. Therefore, we can use this model to further predict the signal enhancement we obtain by introducing an RF reflection at Port 1.

Fig. 4 plots the model prediction of the interference signal strength based on the model parameters used to fit the measurement data in Fig. 2. The signal enhancement (without 50 Ω termination versus with termination) is about 4–10 dB, significant, but not spectacular. Nevertheless, this is a proof-of-principle demonstration that efficient bidirectional EOM modulation can be realized using RF reflection, leading to signal enhancement in SA-FSI systems. The signal enhancement would be much greater if the high RF power loss through the EOM could be reduced. Alternatively, one could feed another RF signal to Port 1, instead of using reflection.

B. Experiment on Sensor Multiplexing

Using the SA-FSI with the bi-directional EOM operating more efficiently, we perform multiplexing of weak FBGs in an array. The array consists of 15 weak FBGs, each having a reflectance of a few percent. The reflectances of the FBGs are not strictly controlled during the fabrication process, resulting in some variability from grating to grating. For example, the 4^{th} grating has a maximum peak reflection of 6.2%, while the 8^{th} grating has a peak reflection of only 1.4%. The 15 gratings have alternating peak reflection wavelengths of 1549.43 nm and 1553.45 nm. The spacing between them is approximately 15 cm, with the exception of the spacing between the 12^{th} and the 13^{th} grating, which is intentionally made small (∼8 cm) for testing the spatial resolution of the interrogation system.

The SA-FSI system is shown in Fig. 1(a), and the two testing arrangements are shown in Fig. 1(b) and 1(c). An ASE source with an output power of ∼15 mW is used as the source. The insertion loss of the circulator is ∼1 dB and the insertion loss of the EOM is ∼4 dB per pass. The forward and backward (i.e., reflected) lightwaves are modulated by the EOM described in the previous section. The RF power is applied in the backward direction (to RF Port 2) without termination at Port 1 (open circuit). The RF frequency is tuned from 2 to 8 GHz, due to the bandwidth limitation of our RF amplifier. The EOM is biased at the quadrature point for the forward propagating lightwave stabilized by a power stabilization module (MBC-MZM-01). The bias voltage is dynamically adjusted to compensate any thermal drift of the EOM by detecting a 1% shunt feedback power. The spectral measurement was done using a tunable filter (JDSUniphase TB9) which is placed in front of the PD. Two measurement ranges were tested, with the FBG arrays placed at around 6.5 m and 1017 m from the EOM, the larger distance is used to verify that SA-FSI is capable of a large sensing range.

For the short-range test (Fig. 1(b)), the RF frequency scanning step (f_{step}) is chosen to be 1 MHz. After fast Fourier Transform (FFT) of the acquired interference signal (I_v), the result is shown in Fig. 5(a). Note, because we used a broadband source, all gratings reflect parts of the broad spectrum, and therefore all gratings are "visible" after applying FFT. The peak amplitude variation reflects the variability in grating reflectances. The locations of the 15 FBGs revealed after FFT are: 5.572 m, 5.736 m, 5.873 m, 6.049 m, 6.196 m, 6.340 m, 6.473 m, 6.627 m, 6.740 m, 6.886 m, 7.054 m, 7.203 m, 7.281 m, 7.417 m, and 7.589 m. The separations between FBGs measured by the SA-FSI are in close agreement with the expected values estimated from the FBG fabrication process. In particular, the

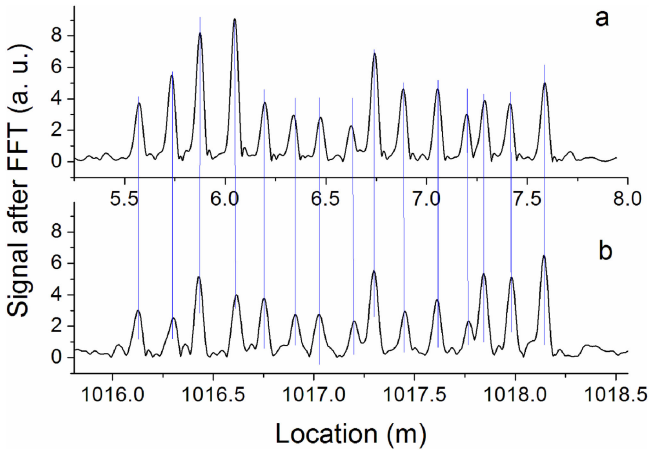

Fig. 5. The SA-FSI signal obtained after FFT of the interference signal acquired by the photodiode for the 15-FBG array when it is placed (a) 6.5 m away and (b) 1 km away from the EOM.

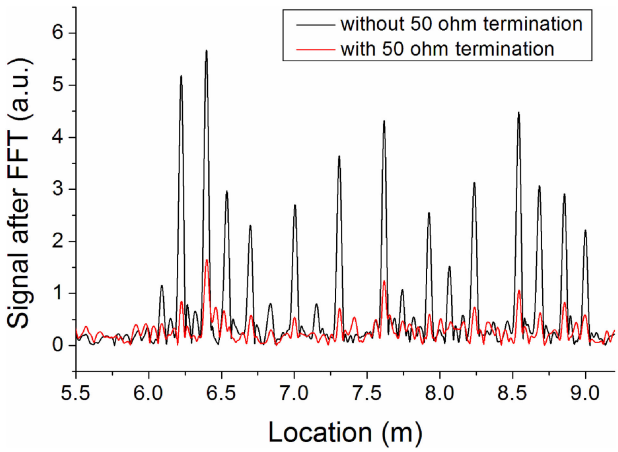

Fig. 6. The SA-FSI signal obtained after FFT of the interference signal acquired by the photodiode with a set of 18-FBG array with (red) and without (black) the matching termination impedance at the EOM port 1.

shortest spacing is measured between the 12th and 13th gratings, which is a 7.8 cm. At this separation, the two peaks are still clearly resolved. The reflection peak width (FWHM) from Fig. 5(a) is ~3 cm, demonstrating the spatial resolution of the SA-FSI system.

We also note that the SNR in Fig. 5(a), defined as the ratio of the highest peak signal to the average background level, is 18 dB, which is quite high considering the low ASE power, the high loss components, and that there is no optical amplification. Compared with the SA-FSI results reported in [16] where RF reflection is not introduced in the EOM, the SNR presented here is larger despite the fact that the reflected optical signal is at least 15 dB weaker due to the narrow-band FBGs used here and the insertion loss of the tunable filter. This further shows that RF reflection can enhance the SA-FSI signal strength. As a direct demonstration of the enhancement of introducing RF reflection in the EOM, we show in Fig. 6(a) comparison of measurements taken with and without the EOM termination impedance. It can be seen that the enhancement factor observed experimentally

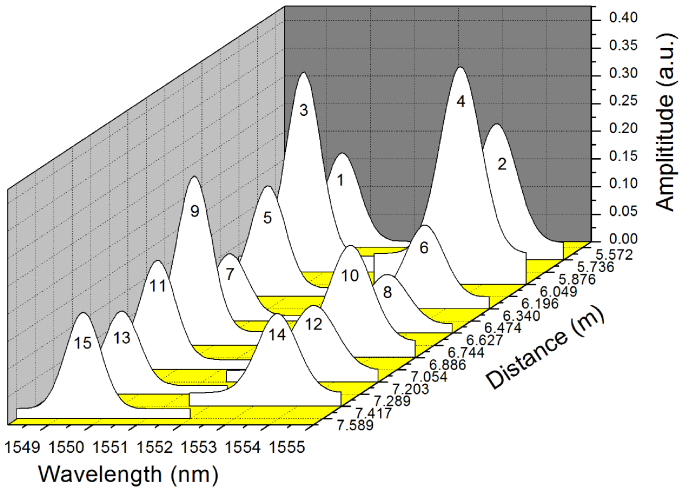

Fig. 7. The reflection spectra of 15 FBGs measured by bidirectional SA-FSI system shown in Fig. 1. The spectra shown are smoothed using a Guassian fit of experimental spectra. The SA-FSI system measures all 15 FBGs simultaneously.

(Fig. 6) is in agreement with the 4–10 dB enhancement predicted by the model.

For the longer sensing range of 1 km (Fig. 1(c)), a frequency step $f_{\text{step}} = 0.1$ MHz was selected. The measurement result is shown in Fig. 5(b). Compared with the short-range result above (Fig. 5(a)), it can be seen that all peaks separations resulting from the two measurements are consistent. The variation in peak reflectances between the two measurements can be attributed to polarization variation due to different fiber placement, as the EOM we use are polarization dependent. There is a slight deterioration in SNR for the long-range measurement, as expected. Nevertheless, the reflection peak can be distinguished manifestly from the noise, and the relative position of each peak is highly consistent with that of the short-range result. The above results indicated that the existing SA-FSI can achieve distributed detection of weak reflection points with a one-kilometer range and a spatial resolution of a couple of centimeters.

The high spatial resolution achieved using 6 GHz of frequency sweep range is essential for certain quasi-distributed sensing applications [21] when such spatial resolution is difficult to achieve using the TDM technology. The high SNR achieved without optical amplification is an additional advantage compared to the TDM technology.

We have further measured the reflection spectra of all FBGs using a tunable filter (JDSUniphase TB9) before the detector. The tunable filter has a FWHM bandwidth of 0.22 nm and a tuning resolution of 0.01 nm. This is the first time spectrally resolved SA-FSI was demonstrated. The measured spectra of all 15 FBGs were smoothed with a Gaussian fit function and shown in Fig. 7. The spectral resolution of the system is limited by the reflection bandwidth (~1 nm) of the FBGs, due to the short length (~1 mm) of the FBGs. Although the detected power after the tunable filter was greatly reduced, we are still able to obtain unambiguous location-resolved FBG spectra with high SNR (Fig. 7).

One limitation of FSI is its measurement speed, as the method requires sweeping the RF frequency and sweeping the tunable

filter. The measurement time is mainly limited by the time it takes to complete RF and wavelength sweeps. (That is, for each RF frequency, the tunable filter will be swept. Alternatively, for each tunable filter setting, the RF frequency will be swept). For the RF source (HP83620B) used here, it takes about 6 s to complete each RF sweep for the short-range measurement (6000 RF steps), and 60 s for the 1 km measurement. The overall measurement time depends on how many wavelength points are taken. Note that, if we use a fast-sweeping RF source, the measurement time can be drastically shortened. Also, a fast-scanning tunable filter with kHz scanning speed can be used [22], further shorten the measurement time. A detailed discussion on measurement speed for FSI can be found in [22]. On the positive side, all of the FBGs are interrogated simultaneously.

IV. Conclusion

We have shown that the SA-FSI technology is capable of achieving cm-level spatial resolution by employing a bidirectional EOM operating in multi-gigahertz range. We experimentally demonstrate that the EOM can be made to modulate lightwaves propagating in both directions efficiently by removing the 50 Ω impedance termination. This results in a reflection of the applied RF wave, which facilitated the modulation of the lightwave bi-directionally, producing a significant signal enhancement. We have also developed a model for EOM modulation in the presence of reflection and optical-RF speed mismatch. Our model provides a tool for designing more efficient bidirectional EOM operation in the future. The SA-FSI employing this bidirectional EOM enabled us to perform spectrally-resolved weak FBG multiplexing using a low power (mW) incoherent broadband source without optical amplification, with a spatial resolution of $\sim$3 cm and a spatial sensing range of $>$1 km.

References

[1] S. J. Mihailov, "Fiber Bragg grating sensors for harsh environments," *Sensors*, vol. 12, no. 2, pp. 1898–1918, Feb. 2012.

[2] G. Laffont, R. Cotillard, and P. Ferdinand, "Multiplexed regenerated fiber Bragg gratings for high-temperature measurement," *Meas. Sci. Technol.*, vol. 24, no. 9, Jul. 2013, Art. no. 094010.

[3] D. Kinet *et al.*, "Fiber Bragg grating sensors toward structural health monitoring in composite materials: Challenges and solutions," *Sensors*, vol. 14, no. 4, pp. 7394–7419, Apr. 2014.

[4] G. Xin *et al.*, "Distributed sensing technology of high-spatial resolution based on dense ultra-short FBG array with large multiplexing capacity," *Opt. Express*, vol. 25, no. 23, Nov. 2017, Art. no. 028112.

[5] F. Ye *et al.*, "Frequency-shifted interferometry: A versatile fiber-optic sensing technique," *Sensors*, vol. 14, pp. 10977–11000, Jun. 2014.

[6] F. Ye, L. Qian, and B. Qi, "Multipoint chemical gas sensing using frequency-shifted interferometry," *J. Lightw. Technol.*, vol. 27, no. 23, pp. 5356–5364, Dec. 2009

[7] O. Yiwen *et al.*, "Large-capacity multiplexing of near-identical weak fiber Bragg gratings using frequency-shifted interferometry," *Opt. Express*, vol. 23, no. 24, Nov. 2015, Art. no. 031484.

[8] K. de Morais Sousa *et al.*, "Fiber Bragg grating temperature sensors in a 6.5-MW generator exciter bridge and the development and simulation of its thermal model," *Sensors*, vol. 14, no. 9, pp. 16651–16663, Sep. 2014.

[9] M. Wang *et al.*, "A large serial time-division multiplexed fiber Bragg grating sensor network," *J. Lightw. Technol.*, vol. 30, no. 17, pp. 2751–2756, Sep. 2012.

[10] J. Huang *et al.*, "Spatially continuous distributed fiber optic sensing using optical carrier based microwave interferometry," *Opt. Express*, vol. 22, no. 15, Jul. 2014, Art. no. 018757.

[11] K. Yuksel *et al.*, "A quasi-distributed temperature sensor interrogated by optical frequency-domain reflectometer," *Meas. Sci. Technol.*, vol. 22, no. 11, Sep. 2011, Art. no. 115204.

[12] O. Yiwen *et al.*, "Large WDM FBG sensor network based on frequency-shifted interferometry," *IEEE Photon. Technol. Lett.*, vol. 29, no. 6, pp. 535–538, Mar. 2017.

[13] F. Ye *et al.*, "Using frequency-shifted interferometry for multiplexing a fiber Bragg grating array," *IEEE Photon. Technol. Lett.*, vol. 20, no. 17, pp. 1488–1490, Sep. 2008.

[14] B. Qi *et al.*, "Frequency-shifted Mach–Zehnder interferometer for locating multiple weak reflections along a fiber link," *IEEE Photon. Technol. Lett.*, vol. 18, no. 1, pp. 295–297, Jan. 2006.

[15] B. Qi, F. Ye, L. Qian, and H. Lo, "Reflectometry based on a frequency-shifted interferometer using sideband interference, "*Opt. Lett.*, vol. 38, no. 7, pp. 1083–1085, Mar. 2013.

[16] Y. Zhang *et al.*, "Multipoint sensing with a low-coherence source using single-arm frequency-shifted interferometry," *Appl. Opt.*, vol. 55, no. 21, pp. 5526–5530, Jul. 2016.

[17] R. A. Becker, "Traveling-wave electro-optic modulator with maximum bandwidth-length product," *Appl. Phys. Lett.*, vol. 45, no. 1, pp. 1168–1170, 1984.

[18] Y. Shi *et al.*, "High-speed electrooptic modulator characterization using optical spectrum analysis," *J. Lightw. Technol.*, vol. 21, no. 10, pp. 2358–2367, Oct. 2003.

[19] A. Wiberg, P. Pérez-Millán, M. V. Andrés, and P. O. Hedekvist, "Microwave-photonic frequency multiplication utilizing optical four wave mixing and fiber Bragg gratings," *J. Lightw. Technol.*, vol. 24, no. 1, pp. 329–334, Jan. 2006.

[20] E. L. Wooten *et al.*, "A review of lithium niobate modulators for fiber-optic communications systems," *IEEE J. Sel. Topics Quantum Electron.*, vol. 6, no. 1, pp. 69–82, Jan./Feb. 2000.

[21] J.-G. Deng *et al.*, "Hot-spot temperature and temperature decay rate measurement in the oil immersed power transformer through FBG based quasi-distributed sensing system," *Microw. Opt. Technol. Lett.*, vol. 59, no. 2, pp. 472–475, Feb. 2017.

[22] F. Ye, "Frequency-shifted interferometry for fiber-optic sensing," Ph.D. dissertation, Dept. Elect. Comput. Eng., Univ. Toronto, Toronto, ON, Canada, 2013, ch. 4.

Authors' biographies not available at the time of publication.